Performance analysis of envelope modelling applied to resonant converters

M. Bertoluzzo , S. Giacomuzzi, and M. Forato

***Abstract*— The paper deals with the analysis of the characteristics of the resonant converters that make them suitable to be modelled and studied using the envelope approach, which is based on the hypothesis that the converters process in a liner way the envelope of the input quantities. The Modulated Variable Laplace Transform method is reviewed and applied to find the envelope model of a wireless power transfer battery charger, considered as study case converter; then it is shown that in certain conditions the envelope model fails in reproducing the system behavior because the latter one performs a non linear processing of the input envelopes. Different types of not linearity are recognized, and the causes of each of them are investigated, detailing the characteristics of the transfer function of the converter that make it more or less suitable for an envelope modelling. The qualitative evaluation of the results coming from the simulation of the study case system is carried out in parallel to the development of a general mathematical analysis of the behavior of a system supplied by a modulated quantity so that each step of the latter one is validated before going ahead to the next and the obtained results can be applied to any kind of system.**

Keywords—envelope models, resonant converter, frequency analysis

I. INTRODUCTION

A large number of power converter topologies makes profitably use of resonance to enhance the performance of the circuit. In these systems, a resonant network formed by two or more reactive elements is supplied by a switching square wave voltage commutating at the resonance frequency or near to it; thanks to the resonance, a nearly sinusoidal current flows through the resonant network. Very often, the resonant frequency is so high that the switching frequency of the converter and the sampling rate of its controller are not enough to implement techniques such as the PWM to perform an effective control of the instantaneous values of the alternate quantities. Fortunately, such a control is not required and it is enough to control their peak amplitude, or envelope, to implement the requested functions because the actual waveforms of the circuit quantities are mostly dictated by the resonant behavior of the circuit. In this context, the analysis of the converter functioning, rather than considering the instantaneous values of the involved electric quantities, is based on the envelopes of the alternate quantities and, if necessary, on the average values over a supply period of the continuous ones.

When envelopes are considered in place of instantaneous values, the conventional transfer function (TF) used to describe the behavior of the converter cannot be used; instead, the so-called envelope model (EM), that links the envelope of the input signal to that of the output one must be introduced.

The Generalized State Space Average (GSSA) [1], [2] is the method most cited in literature to obtain the EM of any kind of system. It is based on the idea that the input quantity is a high frequency modulated sinusoid whose modulating frequency is much lower than that of the carrier; the hypothesis is made that all the other quantities involved in the system functioning have the same kind of waveform or, if they are continuous, vary very slowly with respect to the carrier of the input signal. The whole system is modeled using the state space approach considering as state variables the envelopes of the real signals. The derivative operator used in working out the EM introduces the imaginary variable i so that the state variables have real and imaginary parts; they are considered separately in writing the state space equations and consequently the dimension of the EM is twice that of the original system.

A different approach, known as Laplace Phasor Transform (LPT) is more focused on the analysis of electric or electronic circuits [3]-[5]. It still hypothesizes that the quantities involved in the circuit functioning are amplitude-modulated sinusoids, but studies them applying the phasors. In particular, LPT recognizes that the magnitude of the phasor relevant to a circuital quantity is proportional to its envelope and develops a transformed version of the original circuit where each circuital element operates on the phasors rather than on the original quantities. Differently from GSSA, the LPT method works out directly the envelope TF (ETF) that links the envelope of the output quantity to the that of the input one. As a consequence of computing the magnitude of the phasors, the degree of the denominator of the obtained ETF is twice that of the original one, like it happens with GSSA.

Recently, the method of the Modulated Variables Laplace Transform (MVLT) has been proposed [6], [7] to study resonant circuits like the wireless power transfer battery charger. Like the LPT method, the MVLT starts considering the phasors of the quantities related to the circuit functioning, but obtains the input-output ETF exploiting the properties of the Laplace transform (L-transform) operator, without manipulating the single elements of the circuit. In [8] it is demonstrated that the three methods applied to a linear circuit originate the same EM, described by the state matrixes in GSSA and by the ETFs in LPT and MVLT.

The common characteristics of the three methods is to develop the EM considering only the first harmonic of the alternate quantities at the input of the system and to suppose that the output quantities can be represented accurately in the same way, provided that the modulation frequency is low enough. However, no indications are given about the maximum allowable modulation frequency or about the characteristic of the original system that make it more or less suitable to be

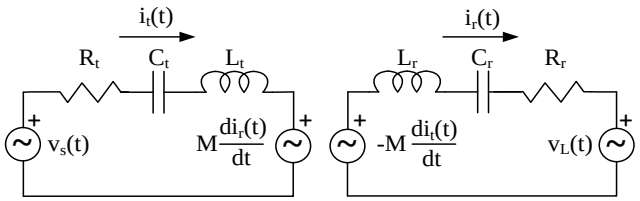

Fig. 1. Study case resonant converter.

accurately represented by the obtained EM. This paper analyzes these aspects and gives some criterions that allow to assess the accuracy of the EM obtained from any of the considered methods without actually developing it, but only by inspection of the Bode diagrams of the TFs original system. Moreover, the paper recognizes three classes of differences between the envelopes computed by the EM and those of the quantities relevant to the original system and investigates the cause of each of them reaching general results that hold for any kind of system.

The paper is organized as follows: Section II introduces the study case system. Section III reviews the MVLT method. Section IV applies the MVLT method to the study case system and checks the accuracy of the obtained EM discovering that the original systems performs a nonlinear processing on the envelopes of the input quantities. Section V analyzes the cause of the non-linearity and summarizes the conditions by which the system operates linearly on the envelopes and can be accurately represented by an EM. Section VI concludes the paper.

In the following discussion, sinusoidal or modulated quantities are denoted as functions of the time using lower case letters; their envelopes are denoted as function of the time using lower case letters with a hut; phasors are complex functions of the time and are denoted with lower case letters with a bar. The L-transforms of the previous quantities are denoted as functions of the variable s using plain upper-case letters, upper case letters with a hut, or upper-case letters with a bar, respectively. The term peak amplitude is used for sinusoidal quantities while the term envelope is used for modulated quantities, i.e. for quantities whose peak amplitude is not constant.

II. Study Case Converter

The study case converter is a wireless battery charger for electric vehicles. Considering only its main features, it can be schematized as in Fig. 1. It is formed by two coupled coils, deployed respectively on the ground and onboard the vehicle, represented by their self-inductances L_t and L_r, by their parasitic resistances R_t and R_r, and by their mutual inductance M. A high frequency inverter supplies the transmitting coil with a square wave voltage $v_s(t)$ and injects in the coil the current $i_t(t)$. Due to the flux linkage between the coils, a voltage is induced across the receiving coil that forces the current $i_r(t)$ in the load. The latter one is constituted by the cascade of a diode rectifier, a dc-dc converter and the vehicle battery. In the hypothesis of having a continuous flow of $i_r(t)$ and a constant voltage at the output of the diode rectifier, the load can be represented by the square wave voltage generator $v_L(t)$. Capacitors C_t and C_r are connected in series to the coils to minimize the sizing power and to maximize the efficiency of the battery charger, respectively [9]. The L-C series performs a band-pass action so that both $i_t(t)$ and $i_r(t)$ are nearly sinusoidal and only the first harmonics of $v_s(t)$ and $v_L(t)$can be considered in studying the circuit without impairing the correctness of the results. The envelope $\hat{\imath}_r(t)$ of the current $i_r(t)$, which indirectly charges the battery through the diode rectifier and the chopper, is controlled acting on the envelope $\hat{v}_s(t)$ of the first harmonic component of $v_s(t)$. The design of the control algorithm for such a system requires to know the ETF that links $\hat{I}_r(s)$ to $\hat{V}_s(s)$ while the prediction and the avoidance of undue solicitation of the inverter and of the transmitting coil requires to know the ETF from $\hat{V}_s(s)$ to $\hat{I}_s(s)$. For these reasons, the wireless power transfer systems are good candidates for the use of an envelope model in designing their control algorithms and in studying their functioning and performance.

From the circuit in Fig. 1 the TFs from $V_s(s)$ to $I_t(s)$ and from $V_s(s)$ to $I_r(s)$ are readily found and result in

$$G_{I_t}(s) \triangleq I_t(s)/V_s(s) = \frac{D_{n,t}s^3+C_{n,t}s^2+B_{n,t}s}{E_d s^4+D_d s^3+C_d s^2+B_d s+A_d} \quad (1)$$

$$G_{I_r}(s) \triangleq I_r(s)/V_s(s) = \frac{D_{r,t}s^3}{E_d s^4+D_d s^3+C_d s^2+B_d s+A_d} \quad (2)$$

with the polynomials' coefficients given by

$$\begin{aligned} D_{n,t} &= C_r C_t L_r & A_d &= 1 \\ C_{n,t} &= C_r C_t R_r & B_d &= C_r R_r + C_t R_t \\ B_{n,t} &= C_t & C_d &= C_r L_r + C_t L_t + C_r C_t L R_r R_t \\ D_{r,t} &= -C_r C_t & D_d &= C_r C_t L_r R_t + C_r C_t L_t R_r \\ & & E_d &= C_r C_t L_r L_t - C_r C_t M^2 \end{aligned} \quad (3)$$

The TFs from $V_L(s)$ to $I_t(s)$ and from $V_L(s)$ to $I_r(s)$ have expressions equal to the previous ones but are exchanged each other, so that (1) links $V_L(s)$ to $I_r(s)$ and (2) links $V_L(s)$ to $I_t(s)$. In a real application the amplitude of $v_L(t)$ is nearly constant or slowly variable, so that $v_L(t)$ acts on the system as a disturbance and will not be considered further.

Considering the parameters of a prototypal wireless battery charger [10] reported in Tab. I, the Bode diagrams plotted in Fig.2 relevant to (1) and (2) are obtained. The vertical axis of the magnitude diagram is given in dB and that of the phase diagram in degrees. The horizontal axes of both the diagrams are normalized to the supply angular frequency. The latter one is denoted as ω_c because it corresponds to the carrier angular

TABLE I
STUDY CASE SYSTEM PARAMETERS

Parameter	Symbol	Value
Transmitting side coil self-inductance	L_T	120 μH
Receiving side coil self-inductance	L_R	120 μH
Transmitting coil parasitic resistance	R_T	0.7 Ω
Receiving coil parasitic resistance	R_R	0.7 Ω
Coils mutual inductance	M	30 μH
Transmitting side resonant capacitor	C_T	30 nF
Receiving side resonant capacitor	C_R	30 nF
Supply angular frequency	ω_c	2π·85000 rad/s

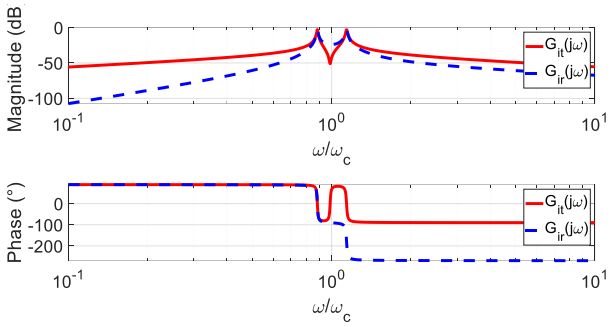

Fig. 2. Bode diagrams of the TFs from $G_{I_t}(s)$ and $G_{I_r}(s)$.

frequency of all the quantities involved in the system functioning. The magnitude diagram clearly shows the peak of resonance of $G_{I_t}(s)$ near to the supply frequency and two additional lateral peaks pertaining to both the TFs. In the study case converter, the resonant frequency is about $0.985\omega_c$. This is an incidental condition caused by the impossibility of realizing the exact resonant capacitance using commercially available capacitors. However, operating slightly out of resonance must not be considered a peculiarity of the study case converter because the capacitors in wireless battery chargers are often sized to present an inductive load to the supply inverter to smoothen its commutations [11].

III. Envelope Model

In this paper MVLT method is considered because its application is rather simple and it furnishes directly the ETF of the system under analysis by manipulating its TF, which usually is known or not so difficult to obtain. TFs are usually written as functions of the variable s that, in this context, represents the derivative operator rather than a numeric value. Further to this consideration, in applying the MVLT method s is considered as a real variable; the same approach is followed also by the LPT method [12].

The development of the EM starts from the consideration that a modulated quantity can be expressed as

$$x(t) = \hat{x}(t)cos\big(\omega_c t + \theta_{x,c}\big), \tag{4}$$

with $\hat{x}(t) > 0$ being the envelope of $x(t)$ and ω_c and $\theta_{x,c}$ the angular frequency and the initial phase of its carrier. Differently from [4], here $\theta_{x,c}$ is not considered equal to zero, so that a more general discussion is given.

The quantity $x(t)$ is considered as the real part of a phasor having slowly variable magnitude equal to $\hat{x}(t)$ and rotating with angular frequency ω_c on the complex plane. According to this point of view, $x(t)$ is expressed as

$$x(t) = \mathbb{R}e\big[\hat{x}(t)e^{j(\omega_c t+\theta_{x,c})}\big] = \mathbb{R}e[\bar{x}(t)e^{j\omega_c t}] \tag{5}$$

where $\mathbb{R}e[\cdot]$ is an operator that gives the real part of its argument. The rightmost expression in (5) is obtained by defining the complex amplitude $\bar{x}(t)$ as

$$\bar{x}(t) \triangleq \hat{x}(t)e^{j\theta_{x,c}}, \tag{6}$$

A graphical equivalent of the relation (6) existing between $\bar{x}(t)$ and $\hat{x}(t)$ is given in Fig. 3, where the considered quantities are represented in the synchronous reference frame R0. Symbols t_{min} and t_{max} denote the time instants when $\hat{x}(t)$ reaches respectively its minimum and maximum value. According to the figure, once $\bar{x}(t)$ is known, $\hat{x}(t)$ can be worked out either from the magnitude of $\bar{x}(t)$ or rotating it counterclockwise of the angle $\theta_{x,c}$, as can be derived also from (6). The first approach is at the basis of the MVLT discussion in [4]; here, instead, the second approach will be followed because it leads to the same result, but does not require to introduce the hypothesis of operating with small signals.

When $x(t)$ is applied at the input of a linear system described by the transfer function $G(s)$, at the system output is generated $y(t)$. The latter one is a modulated quantity having the same carrier angular frequency as $x(t)$ and expressed as

$$y(t) = \hat{y}(t)cos\big(\omega_c t + \theta_{y,c}\big) \tag{7}$$

where $\hat{y}(t) > 0$ is the envelope of y(t) and $\theta_{y,c}$ is the initial phase of its carrier; both of them depending on $x(t)$ and on $G(s)$. In particular, it is

$$\theta_{y,c} = \theta_{x,c} + \theta_{G,\omega_c}, \tag{8}$$

where θ_{G,ω_c} is the phase delay introduced at steady state by $G(s)$ when the system is supplied by a sinusoidal signal having angular frequency ω_c.

Expressions (5) and (6) hold also for $y(t)$ so that the envelope $\hat{y}(t)$ is obtained by rotating counterclockwise of the angle $\theta_{y,c}$ the complex amplitude $\bar{y}(t)$, according to

$$\hat{y}(t) = \bar{y}(t)e^{-j\theta_{y,c}} \tag{9}$$

Considering the phasors instead of the scalar quantities, one can say that if the system is supplied with the phasor $\bar{x}(t)e^{j\omega_c t}$, at its output appears the phasor $\bar{y}(t)e^{j\omega_c t}$, whose complex amplitude and initial phase are represented in Fig. 3. Using the Laplace notation, the relation between input and output phasors is written as

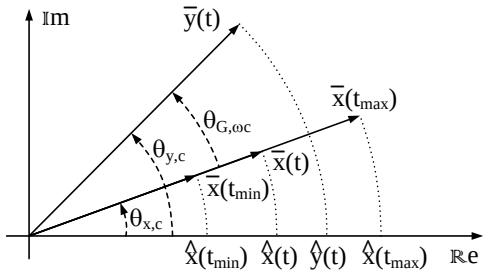

Fig. 3. Relation between peak amplitude $\hat{x}(t)$ and the complex amplitude $\bar{x}(t)$.

$$\mathfrak{Q}[\bar{y}(t)e^{j\omega_c t}] = G(s)\mathcal{L}[\bar{x}(t)e^{j\omega_c t}], \quad (10)$$

where $\mathcal{L}[\cdot]$ is the L-transform operator.

Exploiting the frequency shifting property of the L-transform, (10) is rewritten as

$$\bar{Y}(s - j\omega_c) = G(s)\bar{X}(s - j\omega_c), \quad (11)$$

where $\bar{X}(\cdot)$ and $\bar{Y}(\cdot)$ are the L-transforms of the input and output complex amplitudes, respectively.

Finally, operating a change of variable, the relation between the L-transforms of the two complex amplitudes is simplified in

$$\bar{Y}(s) = G(s + j\omega_c)\bar{X}(s). \quad (12)$$

In a physical system, the envelope $\hat{y}(t)$ of the output quantity is real and consequently its L-transform $\hat{Y}(s)$ is real as well. From (9), the latter one can be expressed as

$$\hat{Y}(s) = \bar{Y}_{\mathbb{R}e}(s)cos\theta_{y,c} + \bar{Y}_{\mathbb{I}m}(s)sin\theta_{y,c}, \quad (13)$$

obtained denoting with $\bar{Y}_{\mathbb{R}e}(s)$ and $\bar{Y}_{\mathbb{I}m}(s)$ the real and the imaginary parts of $\bar{Y}(s)$, respectively.

Like $\hat{y}(t)$ and $\hat{Y}(s)$, also the input quantity $\hat{x}(t)$ and its L-transform $\hat{X}(s)$ are real so that, from (6), the real and imaginary parts of $\bar{X}(s)$ are separated and result in

$$\begin{matrix} \bar{X}_{\mathbb{R}e}(s) = \hat{X}(s)cos\theta_{x,c} \\ \bar{X}_{\mathbb{I}m}(s) \triangleq \hat{X}(s)sin\theta_{x,c} \end{matrix}. \quad (14)$$

Operating the separation also on $G(s + j\omega_c)$, from (12) and (14) the following relations are obtained:

$$\begin{matrix} \bar{Y}_{\mathbb{R}e}(s) = \hat{X}(s)\left[G_{\mathbb{R}e}(s + j\omega)cos\theta_{x,c} - G_{\mathbb{I}m}(s + j\omega s)sin\theta_{x,c}\right] \\ \bar{Y}_{\mathbb{I}m}(s) = \hat{X}(s)\left[G_{\mathbb{R}e}(s + j\omega)sin\theta_{x,c} + G_{\mathbb{I}m}(s + j\omega)cos\theta_{x,c}\right] \end{matrix}. \quad (15)$$

Substituting (15) in (13) gives

$$\frac{\hat{Y}(s)}{\hat{X}(s)} = G_{\mathbb{R}e}(s + j\omega)cos\left(\theta_{y,c} - \theta_{x,c}\right) + G_{\mathbb{I}m}(s + j\omega)sin\left(\theta_{y,c} - \theta_{x,c}\right), \quad (16)$$

and finally, using (8), the ETF is obtained in the form

$$\hat{G}(s) \triangleq \frac{\hat{Y}(s)}{\hat{X}(s)} = \mathbb{R}e\left[G(s + j\omega_c)e^{-j\theta_{G,\omega_c}}\right]. \quad (17)$$

The computation of the real part of the argument between brackets in (17) involves its rationalization so that the resulting degree of the denominator of $\hat{G}(s)$ is twice that of $G(s)$, as it happens with GSSA and LPT methods.

IV. Envelope Model accuracy test

Application of (17) to the TF of a resonant converter, even if as simple as that one chosen as study case, leads to very complex expressions, such as that given in (18)

$$\hat{G}_{i_t}(s) \triangleq \frac{\hat{I}_t(s)}{\hat{V}_s(s)} = \frac{\hat{H}_{n,t}s^7 + \hat{G}_{n,t}s^6 + \hat{F}_{n,t}s^5 + \hat{E}_{n,t}s^4 + \hat{D}_{n,t}s^3 + \hat{C}_{n,t}s^2 + \hat{B}_{n,t}s + \hat{A}_{n,t}}{\hat{I}_d s^8 + \hat{H}_d s^7 + \hat{G}_d s^6 + \hat{F}_d s^5 + \hat{E}_d s^4 + \hat{D}_d s^3 + \hat{C}_d s^2 + \hat{B}_d s + \hat{A}_d} \quad (18)$$

where the polynomial coefficients are functions of the constants given by (3), of $sin\,\theta_{G,\omega_c}$, $cos\,\theta_{G,\omega_c}$, and ω_c; a similar expression is obtained also for $\hat{G}_{i_r}(s) \triangleq \hat{I}_r(s)/\hat{V}_s(s)$. These expressions are hardly useful in obtaining an insight on the characteristics of the EM while the analysis of the correspondent Bode diagrams is more profitable.

In conventional systems, the Bode diagrams are obtained by substituting $j\omega$ to s in the TF and plotting the magnitude and the phase of the obtained complex function of ω. By definition, for each value of ω, the magnitude Bode diagram gives the peak amplitudes of the sinusoidal output obtained when the system is supplied with a sinusoidal input having angular frequency ω and peak amplitude equal to 1; the phase diagrams, instead, give the phase delay of the output with respect to the input. By extension of the conventional approach, the envelope Bode (EBode) diagrams relevant to the outputs $\hat{\imath}_t(t)$ and $\hat{\imath}_r(t)$ are obtained by substituting $j\omega_m$ to s in the ETFs $\hat{G}_{i_t}(s)$ and $\hat{G}_{i_r}(s)$ obtained from (17). In this case, however, it is not possible to suppose that $\hat{v}_s(t)$, $\hat{\imath}_t(t)$, and $\hat{\imath}_r(t)$ have sinusoidal waveforms because they are the envelopes of modulated quantities and hence are by definition positive.

Nevertheless, the EBode diagrams still can be used by considering $\hat{v}_s(t)$ as given by the sum of two contributions according to

$$\hat{v}_s(t) = A_v\left[1 + m_v cos\left(\omega_m t + \theta_{v,m}\right)\right], \quad (19)$$

The constant contribution A_v is hereafter denoted as the carrier component while the sinusoidal contribution is denoted as the modulating component. Considering (4), the first component fixes the amplitude of the carrier of $v_s(t)$ while the second one defines the characteristics of its amplitude modulation, fixing its peak amplitude$A_v m_v$, angular frequency ω_m and initial phase $\theta_{v,m}$. Setting $m_v < 1$ forces $\hat{v}_s(t)$ to be always positive and imposing $\omega_m \ll \omega_c$ assures that $v_s(t)$ falls within the scope of application of MVLT and of the other methods used to develop the Ems.

The envelopes $\hat{\imath}_s(t)$ and $\hat{\imath}_r(t)$ of the output currents are obtained using the superposition of the effects. If only the carrier component is considered, or m_v is set to 0, $v_s(t)$ is a pure sinusoid oscillating with angular frequency ω_c; the corresponding currents $i_t(t)$ and $i_r(t)$ are pure sinusoids as well, with peak amplitudes dictated by the TFs $G_{i_t}(s)$ and $G_{i_r}(s)$ of the original system according to

$$\begin{matrix} \hat{\imath}_s(t) = A_v\left|G_{i_t}(j\omega_c)\right| \\ \hat{\imath}_r(t) = A_v\left|G_{i_r}(j\omega_c)\right| \end{matrix}. \quad (20)$$

If $m_v > 0$, a modulating component is added to both the envelopes $\hat{\imath}_t(t)$ and $\hat{\imath}_r(t)$ and they change into

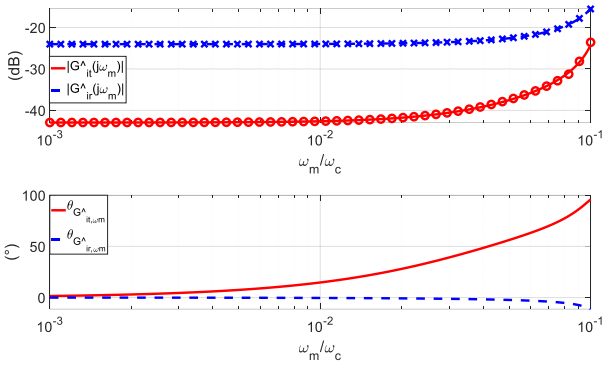

Fig. 4. EBode diagrams obtained from the EM (lines) and envelope gains obtained by simulation (circles for $K_{i_t}(j\omega_m)$ and crosses for $K_{i_r}(j\omega_m)$).

$$\hat{\imath}_t(t) = A_v\left[\left|G_{i_t}(j\omega_c)\right| + m_v\left|\hat{G}_{i_t}(j\omega_m)\right|cos\left(\omega_m t + \theta_{v,m} + \theta_{\hat{G}_{i_t},\omega_m}\right)\right]$$
$$\hat{\imath}_r(t) = A_v\left[\left|G_{i_r}(j\omega_c)\right| + m_v\left|\hat{G}_{i_r}(j\omega_m)\right|cos\left(\omega_m t + \theta_{v,m} + \theta_{\hat{G}_{i_r},\omega_m}\right)\right] \quad (21)$$

.

The peak amplitudes of the modulating components and their phases with respect to the modulating component of $\hat{v}_s(t)$ are derived from the EBode diagrams of the two ETFs shown in Fig. 4. Like in Fig. 2, the horizontal axis is normalized to the supply angular frequency but, in this case, it extends to a shorter interval because of the condition $\omega_m \ll \omega_c$.

The accuracy of the EM expressed by (17) has been checked by comparing the magnitude diagram obtained from the ETFs with those relevant to the real converter obtained by circuital simulations. In this step of the analysis, simulations have been used because they allow to study the system in ideal conditions, with a modulated sinusoidal supply voltage, without the need of discriminating the effects of the high frequency components of the square wave supply voltage generated by the inverter.

A Simulink model has been arranged that encompasses a circuital model of the study case system and two blocks implementing the ETFs $\hat{G}_{i_t}(s)$ and $\hat{G}_{i_r}(s)$. The circuital model is supplied with a modulated voltage with envelope $\hat{v}_s(t)$ expressed by (19), with A_v=1 V, m_v=0.1 and $\theta_{v,m} = \pi/3$ rad, and generates the current outputs $i_t(t)$ and $i_r(t)$. The ETF blocks are supplied with $\hat{v}_s(t)$ and generates $\hat{\imath}_t(t)$ and $\hat{\imath}_r(t)$. Several tests have been performed with ω_m ranging from $0.001\ \omega_c$ to $0.1\ \omega_c$. For each of them, the differences Δ_{it} and Δ_{ir} between the maximum and the minimum of the envelopes of $i_t(t)$ and $i_r(t)$ have been measured, as exemplified in Fig. 5, and recorded. With an accurate EM, Δ_{it} and Δ_{ir} are equal to twice the peak amplitudes of the modulating components of $\hat{\imath}_t(t)$ and $\hat{\imath}_r(t)$ that, from (21), are $A_v m_v\left|\hat{G}_{i_t}(j\omega_m)\right|$ and $A_v m_v\left|\hat{G}_{i_r}(j\omega_m)\right|$. This correspondence has been checked dividing the measured differences by two times the peak amplitude $A_v m_v$ of the modulating component of $\hat{v}_s(t)$ to work out the actual envelope gains $K_{i_t}(j\omega_m)$ and $K_{i_r}(j\omega_m)$ of the real converter; they have been converted in dB and plotted in Fig. 4 using circles for $K_{i_t}(j\omega_m)$ and crosses for $K_{i_r}(j\omega_m)$. The correspondence between the diagrams obtained from the ETFs and the gains from the simulations is very good for both the currents and along the full span of ω_m. So that it can be concluded that the EM is accurate in reproducing the envelope gains of the study case system.

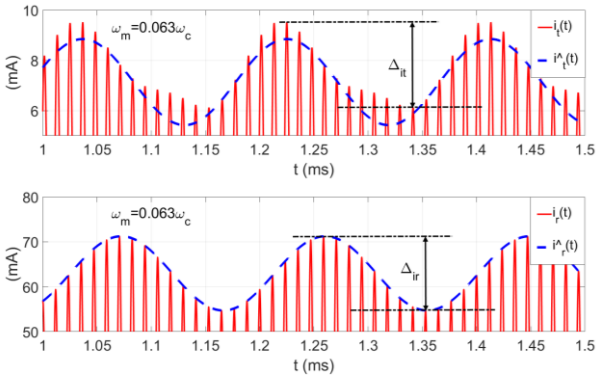

Fig. 5. Currents $i_t(t)$ and $i_r(t)$ and the envelopes $\hat{\imath}_t(t)$ and $\hat{\imath}_r(t)$ obtained with ω_m=0.063 ω_c.

However, an unexpected result comes from the analysis of the waveforms of the currents from the circuital model. Taking as an example those obtained supplying the study case converter with $\omega_m = 0.063\ \omega_c$, reported in Fig. 5, the envelope of $i_t(t)$, appears to be somewhat distorted and hence cannot be reproduced by $\hat{\imath}_t(t)$, which is obtained from a linear EM. Strangely enough, the same result does not happen to $i_r(t)$, whose envelope is sinusoidal and coincides with $\hat{\imath}_r(t)$.This demonstrate that an EM can be accurate in modelling one of the outputs of the system but at the same time can be inadequate when another output of the same system is considered. This

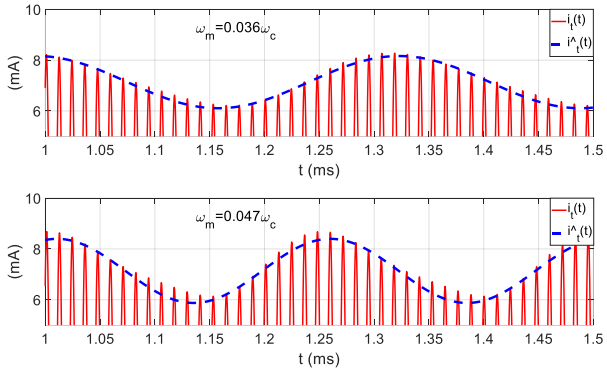

Fig. 6. Current $i_t(t)$ and envelope $\hat{\imath}_t(t)$ obtained with $\omega_m = 0.036\ \omega_c$and $\omega_m = 0.047\ \omega_c$.

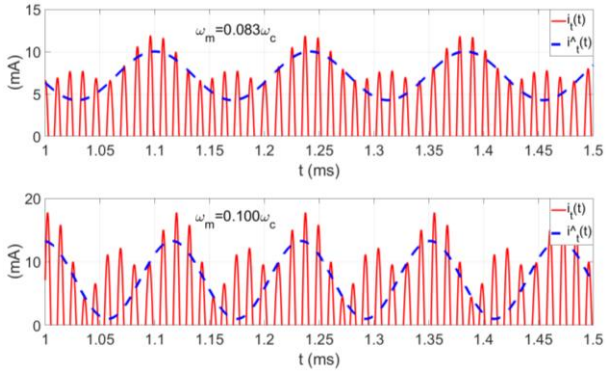

Fig. 7. Current $i_t(t)$ and envelope $\hat{\imath}_t(t)$ obtained with $\omega_m = 0.083\ \omega_c$and $\omega_m = 0.1\ \omega_c$.

limitation is not due to a lack of the EM, but derives from the behavior of the real system that, although being linear when conventional inputs and outputs are considered, processes the envelopes in a nonlinear way so that, strictly speaking, its EM is not more representable through an ETF. Figs. 6 and 7 show that the non-linearity of $\hat{\imath}_t(t)$ with respect to $\hat{v}_s(t)$ worsens as ω_m increases. The envelope $\hat{\imath}_r(t)$ is not reported in the figures because its correspondence with the envelope of $i_r(t)$ results nearly perfect with any value of ω_m up to $0.1\omega_c$.

Besides being distorted, Figs 5, 6 and 7 show that the actual envelopes of $i_t(t)$ reach values higher then $\hat{\imath}_t(t)$. This condition could jeopardize the safety of a wireless battery charger sized using the EM because the actual maximum current at the output of the inverter and flowing in the transmitting coil is higher than that forecasted using the EM.

V. Envelope models Analisys

A. Conditions for a linear processing of the envelopes

The not-linear processing of the envelopes in the real system and the consequent impossibility to work out an accurate EM can be explained analyzing in details the functioning of a linear system supplied by a modulated input. According to Fig. 3, MVLT and the other methods are developed representing the quantities involved in the system operation as phasors whose tips move along a straight-line as the modulating component of their envelopes oscillates. In some situations, this representation is incorrect and leads to the inability to forecast properly the behavior of the system, as discovered in the previous Section.

If the modulating component of $\hat{x}(t)$ is sinusoidal, like in (19), from (4) and using the prostaphaeresis formulas the input of the system can be written as

$$x(t) = A_x cos\big(\omega_c t + \theta_{x,c}\big) + \frac{A_x m_x}{2} cos\big[(\omega_c - \omega_m)t + \theta_{x,c} - \theta_{x,m}\big] + \frac{A_x m_x}{2} cos\big[(\omega_c + \omega_m)t + \theta_{x,c} + \theta_{x,m}\big]. \quad (22)$$

This expression highlights that the input signal encompasses the three components $x_A(t)$, $x_-(t)$, and $x_+(t)$ having angular frequencies ω_c, $\omega_c - \omega_m$, and $\omega_c + \omega_m$, respectively. Each of the components can be derived from a phasor, like in (5), thus defining the three complex amplitudes $\bar{x}_A(t)$, $\bar{x}_-(t)$, and $\bar{x}_+(t)$. The complex amplitude $\bar{x}(t)$ and its components represented in the reference frame R0 are reported in Fig. 8, relevant to the time instant $t = 0$. By definition, the component $\bar{x}_A(t)$ is fixed in R0 while $\bar{x}_-(t)$ and $\bar{x}_+(t)$ rotate respectively clockwise and anticlockwise with angular frequency ω_m . Being the magnitudes of $\bar{x}_-(t)$ and $\bar{x}_+(t)$ equal and their initial phases opposite each to the other with respect to that of $\bar{x}_A(t)$, the tip of $\bar{x}(t)$ lies always on the extension of $\bar{x}_A(t)$, according to the hypothesis at the basis of MVLT.

According to the superposition of the effects, the output of the system can be decomposed into three components, like in (23)

$$y(t) = y_A(t) + y_-(t) + y_+(t). \quad (23)$$

In details, the three components are expressed as

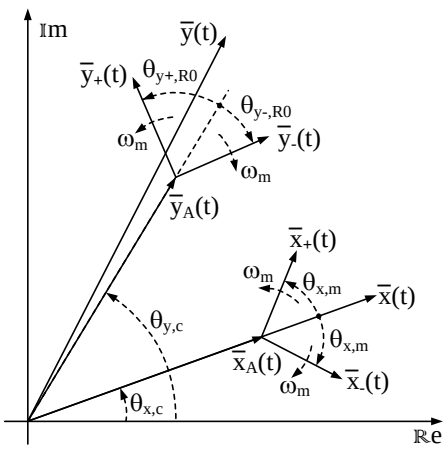

Fig. 8. Components of $\bar{x}(t)$ and $\bar{y}(t)$.

$$\begin{aligned} y_A(t) &= A_x G_{\omega_c} cos\big(\omega_c t + \theta_{x,c} + \theta_{G,\omega_c}\big) \\ y_-(t) &= \tfrac{A_x m_x}{2} G_{\omega_c - \omega_m} cos\big[(\omega_c - \omega_m)t + \theta_{y-,R0}\big], \\ y_+(t) &= \tfrac{A_x m_x}{2} G_{\omega_c + \omega_m} cos\big[(\omega_c + \omega_m)t + \theta_{y+,R0}\big] \end{aligned} \quad (24)$$

with initial phases defined as

$$\begin{aligned} \theta_{y-,R0} &\triangleq \theta_{x,c} - \theta_{x,m} + \theta_{G,\omega_c - \omega_m} \\ \theta_{y+,R0} &\triangleq \theta_{x,c} + \theta_{x,m} + \theta_{G,\omega_c + \omega_m}. \end{aligned} \quad (25)$$

In the same way as with $x(t)$, the components of $y(t)$ are associated to the complex amplitudes $\bar{y}_A(t)$, $\bar{y}_-(t)$, and $\bar{y}_+(t)$ drawn in Fig. 8. The first of them is fixed while $\bar{y}_-(t)$ and $\bar{y}_+(t)$ rotate in opposite directions with angular frequency ω_m . Generally, at the angular frequencies $\omega_c - \omega_m$, and $\omega_c + \omega_m$, the gains $G_{\omega_c - \omega_m}$ and $G_{\omega_c + \omega_m}$ of $G(s)$ and its phase delays $\theta_{G,\omega_c - \omega_m}$ and $\theta_{G,\omega_c + \omega_m}$ do not match; consequently the magnitudes of the components $\bar{y}_-(t)$ and $\bar{y}_+(t)$ are different and their initial position are not symmetrical with respect to $\bar{y}_A(t)$. Then, as $\bar{y}_-(t)$ and $\bar{y}_+(t)$ keep rotating, the phase of $\bar{y}(t)$ changes and it does not stay aligned with $\bar{y}_A(t)$.

Figure 8 gives the hint that the tip of $\bar{y}(t)$ moves on a closed trajectory centered on the tip of $\bar{y}_A(t)$. The analysis on the nature the trajectory is made easier by representing it on a new reference frame, denoted as R1, obtained from the R0 by moving the origin on the tip of $\bar{y}_A(t)$ and rotating the axes to align the real axis with $\bar{y}_A(t)$, as shown in Fig. 9, where the trajectory is sketched with the thick dashed line as an ellipse-like curve.

In the new reference frame, (24) changes into

$$\begin{aligned} &\bar{y}_{A,R1}(t) = 0 \\ &\bar{y}_{-,R1}(t) = A_{y-}\big[cos\big(-\omega_m t + \theta_{y-,R1}\big) + jsin\big(-\omega_m t + \theta_{y-,R1}\big)\big] \\ &\bar{y}_{+,R1}(t) = A_{y+}\big[cos\big(\omega_m t + \theta_{y+,R1}\big) + jsin\big(\omega_m t + \theta_{y+,R1}\big)\big] \end{aligned} , \quad (26)$$

where the magnitudes and the initial phases of $\bar{y}_{-,R1}(t)$ and $\bar{y}_{+,R1}(t)$ are defined according to (27), obtained using (25) and

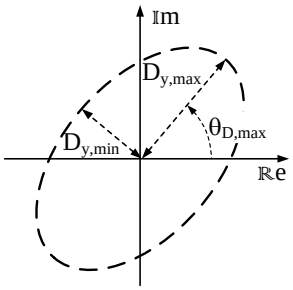

Fig. 9. Trajectory of the tip of $\bar{y}(t)$ in R1.

(8)

$$\begin{aligned} A_{y-} &\triangleq \frac{A_x m_x}{2} G_{\omega_c-\omega_m} \quad \theta_{y-,R1} \triangleq \theta_{y-,R0} - \theta_{y,c} \\ A_{y+} &\triangleq \frac{A_x m_x}{2} G_{\omega_c+\omega_m} \quad \theta_{y+,R1} \triangleq \theta_{y+,R0} - \theta_{y,c} \end{aligned} . \tag{27}$$

In R1, the coordinates of the tip of $\bar{y}(t)$ are

$$\begin{aligned} \bar{y}_{\mathbb{R}e,R1}(t) &= A_{y-}cos(-\omega_m t + \theta_{y-,R1}) + A_{y+}cos(\omega_m t + \theta_{y+,R1}) \\ \bar{y}_{\mathbb{I}m,R1}(t) &= A_{y-}sin(-\omega_m t + \theta_{y-,R1}) + A_{y+}sin(\omega_m t + \theta_{y+,R1}) \end{aligned} \tag{28}$$

and its distance D_y from the origin, obtained after some manipulations, results in

$$D_y = \sqrt{(A_{y-} - A_{y+})^2 + 4A_{y-}A_{y+}cos^2\left(\omega_m t + \frac{\theta_{y+,R1} - \theta_{y-,R1}}{2}\right)}. \tag{29}$$

Using the definitions (27), (29) shows that D_y ranges in the interval $(D_{y,min}, D_{y,max})$ whose extremes are

$$\begin{aligned} D_{y,max} &= A_x m_x \left(\frac{G_{\omega_c-\omega_m} + G_{\omega_c+\omega_m}}{2}\right) \\ D_{y,min} &= A_x m_x \left|\frac{G_{\omega_c-\omega_m} - G_{\omega_c+\omega_m}}{2}\right| \end{aligned} , \tag{30}$$

and are reached when

$$\begin{aligned} \omega_m t_{max} &= \theta_{D,max} + k\pi\,, \quad k \in \mathbb{N} \\ \omega_m t_{min} &= \theta_{D,max} + (k+1)\frac{\pi}{2}, k \in \mathbb{N} \end{aligned} \tag{31}$$

where $\theta_{D,max}$ is the angle between the real axis of R1 and the major axis of the ellipse-like trajectory. It is given by (32), obtained substituting (25) in (27)

$$\theta_{D,max} \triangleq \left(\theta_{G,\omega_c-\omega_m} + \theta_{G,\omega_c+\omega_m}\right)/2 - \theta_{G,\omega_c}. \tag{32}$$

From (28)-(31) and by inspection of Fig. 9 some conclusions can be drawn

C1. if $G_{\omega_c-\omega_m} \neq G_{\omega_c+\omega_m}$,

the trajectory has an ellipse-like form, with the major axis forming and angle equal to $\theta_{D,max}$ with the real axis of R1.

C2. if $G_{\omega_c-\omega_m} = G_{\omega_c+\omega_m}$,

the trajectory collapses into a straight line forming and angle equal to $\theta_{D,max}$ with the real axis of R1.

C3. if $G_{\omega_c-\omega_m} = G_{\omega_c+\omega_m}$ and $\theta_{D,max} = 0$,

the trajectory collapses into a straight line aligned with the real axis of R1.

It can be concluded that condition C3 gives the characteristics of $G(s)$ that assure a linear processing of the envelopes oscillating at angular frequency ω_m. The EM can be accurate only if condition C3 holds because, going back to R0, this is the only condition that keeps the phasor $\bar{y}(t)$ always aligned with $\bar{y}_A(t)$. In conditions C1 and C2 it is not possible to obtain $\hat{y}(t)$ rotating $\bar{y}(t)$ of the fixed angle $\theta_{y,c}$, as in (9), and consequently the modulated component of $\hat{y}(t)$ does not result sinusoidal, the system does not process linearly the envelope of the input signal and the EM fails in forecasting the envelope of the output signal.

Fulfillment of condition C3 by the study case resonant converter for $\omega_m = 0.063\omega_c$ is verified by checking the Bode diagrams of its TFs around the supply angular frequency ω_c using the magnified version of Fig. 2 reported in Fig. 10. Here, the magnitudes and the phases relevant to the angular frequencies ω_c, $\omega_c - \omega_m$, and $\omega_c + \omega_m$ are highlighted using circles for $G_{I_t}(j\omega)$ and crosses for $G_{I_r}(j\omega)$. Inspection of the figure shows that $G_{I_t}(j\omega)$ is about to satisfying condition C2 while $G_{I_r}(j\omega)$, as expected from previous discussion and the results of Section IV, satisfies very well condition C3.

For further confirmation of the correctness of this analysis, the magnitudes and the phases highlighted in Fig. 10 have been inserted in (27) to obtain the parameters of (28). From the latter ones, the trajectories followed by the tips of $\bar{\imath}_t(t)$ and $\bar{\imath}_r(t)$ in R1 have been computed numerically with $\omega_m t$ ranging in the interval $(0, 2\pi)$ and plotted in Fig. 11. The figure confirms that the trajectory of $\bar{\imath}_r(t)$ is nearly a straight-line aligned with the real axis as stated in condition C3. The similarity of the trajectory of $\bar{\imath}_t(t)$with a straight line is not as marked, and, in any case, it is nearly aligned with the imaginary axis, so that condition C3 is not satisfied, thus explaining the nonlinear

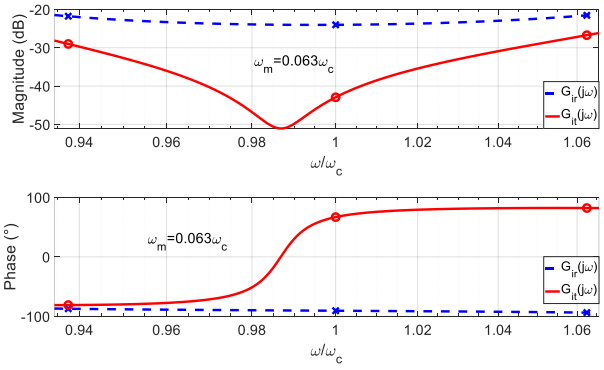

Fig. 10. Magnication of the Bode diagrams of the study case TFs around ω_c.

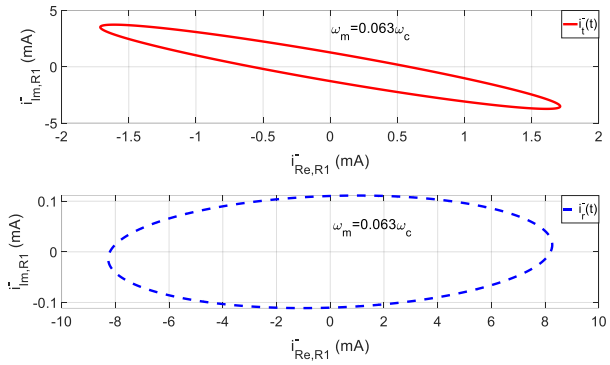

Fig. 11. Trajectories of $\bar{\imath}_t(t)$ and $\bar{\imath}_r(t)$ in R1.

processing of the input envelopes by $G_{I_t}(s)$ and the consequent inaccuracy of the EM.

B. General analysis of the nonlinear envelope processing

Consequences of the failure of $G_{I_t}(j\omega)$ to comply with condition C3 can be qualitatively analyzed by inspection of Figs. 5, 6, and 7. General and quantitative conclusions can be drawn studying the trajectory of the tip of the complex amplitude $\bar{y}(t)$ obtained at the output of a generic system. The study is carried out in a new reference frame, denoted as R2, obtained from R1 by a translation that sets the origin back on that of R0 and maintain the real axis aligned with $\bar{y}_A(t)$. In order to simplify the analysis but without loosing the generality of the results, in the following discussion it is supposed that condition C2 holds so that the trajectory of $\bar{y}(t)$ in R2 is a straight line as in Fig. 12.

According to the figure, as $\omega_m t$ spans the interval $(0, 2\pi)$, the phase of $\bar{y}(t)$ ranges from $\theta_{y,R2,min}$ and $\theta_{y,R2,max}$ and its magnitude changes from Y_{min} to Y_{max} passing through $A_x G_{\omega_c}$, which is the magnitude of $\bar{y}_A(t)$ given by (24).

As seen in Section III, the EM works out $\hat{y}(t)$ by rotating $\bar{y}(t)$ of the constant phase angle $\theta_{y,c}$ to align it with the real axis. In R0, $\theta_{y,c}$ is the phase of the carrier component $\bar{y}_A(t)$ of $\bar{y}(t)$ but in R2, $\bar{y}_A(t)$ is already aligned with the real axis so that no rotation is performed to compute $\hat{y}(t)$ and it simply corresponds to the real part of $\bar{y}(t)$. Consequently, $\hat{y}(t)$ moves in the interval $(\hat{Y}_{min}, \hat{Y}_{max})$ whose extremes are

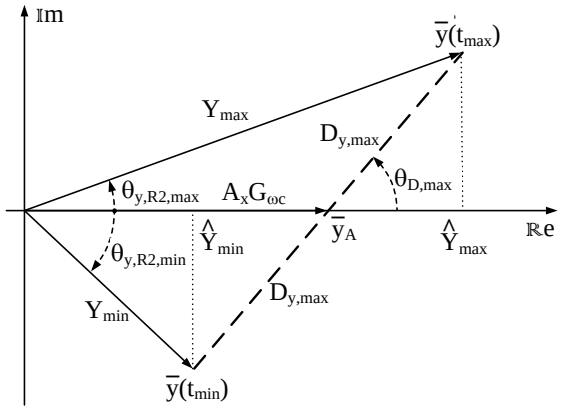

Fig. 12. Trajectory of the tip of $\bar{y}(t)$ in R2 when condition C2 is verified.

$$\begin{aligned}\hat{Y}_{min} &= A_x G_{\omega_c} - D_{y,max} cos(\theta_{D,max}) \\ \hat{Y}_{max} &= A_x G_{\omega_c} + D_{y,max} cos(\theta_{D,max})\end{aligned} \quad (33)$$

Once $\hat{Y}_{min}$ and $\hat{Y}_{max}$ are known, the corresponding values of the magnitude of $\bar{y}(t)$ are readily derived as

$$\begin{aligned}Y_{min} &= \sqrt{\hat{Y}_{min}{}^2 + D_{y,max}{}^2 sin^2(\theta_{D,max})} \\ Y_{max} &= \sqrt{\hat{Y}_{max}{}^2 + D_{y,max}{}^2 sin^2(\theta_{D,max})}\end{aligned} \quad (34)$$

From (34) it is clear that $Y_{min} > \hat{Y}_{min}$ and $Y_{max} > \hat{Y}_{max}$ thus justifying the offset between $\hat{\imath}_t(t)$ and the envelope of $i_t(t)$ found in Figs. 5-7 and, even more interesting, demonstrating that the offset will always be present whenever condition C3 is not satisfied.

From (33) and (34), Y_{min} and Y_{max} can be expressed as

$$\begin{aligned}Y_{min} &= \sqrt{(A_x G_{\omega_c})^2 + D_{y,max}{}^2 - 2A_x G_{\omega_c} D_{y,max} \cos(\theta_{D,max})} \\ Y_{max} &= \sqrt{(A_x G_{\omega_c})^2 + D_{y,max}{}^2 + 2A_x G_{\omega_c} D_{y,max} \cos(\theta_{D,max})}\end{aligned} \quad (35)$$

If condition

$$D_{y,max} > 2A_x G_{\omega_c} \cos(\theta_{D,max}) \quad (36)$$

holds, Y_{min} results larger than $A_x G_{\omega_c}$. In this case, the envelope of $y(t)$ exhibits a maximum equal to Y_{max} at $\theta_{y,R2} = \theta_{y,R2,max}$, a minimum equal to $A_x G_{\omega_c}$ at $\theta_{y,R2} = 0$, and another maximum equal to Y_{min} at $\theta_{y,R2} = \theta_{y,R2,min}$. The presence of two maxima in one period of the envelope of $y(t)$ is confirmed in Fig. 7 and demonstrates that the envelope is actually distorted. More precisely, (36) is a sufficient condition to have the distortion of the envelope, but it is not necessary because distortion appears as soon as condition C3 is not satisfied.

If the carrier component $\bar{y}_A(t)$ has magnitude much higher that its modulating component, i.e. if

$$A_x G_{\omega_c} \gg D_{y,max}, \quad (37)$$

(35) can be approximated as

$$\begin{aligned}Y_{min} &\approx A_x G_{\omega_c} \left\{1 + \frac{1}{2}\left[\frac{D_{y,max}{}^2}{(A_x G_{\omega_c})^2} - \frac{2D_{y,max}\cos(\theta_{D,max})}{A_x G_{\omega_c}}\right]\right\} \\ Y_{max} &\approx A_x G_{\omega_c} \left\{1 + \frac{1}{2}\left[\frac{D_{y,max}{}^2}{(A_x G_{\omega_c})^2} + \frac{2D_{y,max}\cos(\theta_{D,max})}{A_x G_{\omega_c}}\right]\right\}\end{aligned} \quad (38)$$

The difference $Y_{max} - Y_{min}$, denoted as Δ_{i_t} when it has been defined for the current $i_t(t)$ in Fig. 5, corresponds to twice the peak amplitude of the modulating component of the envelope of $y(t)$ and from (38) is approximated as

$$\Delta_y \approx 2D_{y,max}\cos\left(\theta_{D,max}\right), \tag{39}$$

which is exactly the difference $\hat{Y}_{max} - \hat{Y}_{min}$, i.e. twice the amplitude of the modulating component of $\hat{y}(t)$.

The equivalent of Fig. 12 for the study case system is shown in Fig. 13 using the thin lines. Condition (37) is satisfied so that (39) holds and justifies the correspondence found in Fig. 4 between the EBode diagram worked out from the EM and those obtained from the simulation despite the distortion and the offset of the current's envelopes.

Solicitating the study case converter with a signal having $m_v = 0.3$, the quantity $D_{y,max}$ increases three times with respect to the situation presented in Section IV. The new trajectories of the tips of of $\bar{\imath}_t(t)$ and $\bar{\imath}_r(t)$ are reported in Fig. 13 using the thick lines. In this case, (37) does not hold any more and the envelope gain $K_{i_t}(j\omega_m)$ obtained as described in Section IV should not match $\left|\hat{G}_{i_t}(j\omega_m)\right|$ as accurately as when $m_v = 0.1$. This hypothesis is verified in Fig. 14 where the gains obtained with $m_v = 0.3$ are compared with those relevant to $m_v = 0.1$, shown also in Fig. 4, using triangles and circles, respectively. As expected the new gains do not match those obtained in Section IV. The envelope gain $K_{i_r}(j\omega_m)$ is not reported in the figure because it matches with $\left|\hat{G}_{i_r}(j\omega_m)\right|$ nearly perfectly, as expected knowing that $G_{I_r}(j\omega)$ satisfies condition C3.

VI. Conclusions

The paper reviewed the mathematical background of the MVLT method with a more general discussion with respect to the available literature. The MVLT has been applied to a study case resonant converter to work out its EM. Operations of the EM on the envelope of the input signals has been compared with those performed by the real system discovering that an EM is accurate when one of the outputs is considered and inaccurate with respect to the other. The cause of this behavior has been found in the fact that the study case converter, even if behaving linearly when processing the conventional input, becomes nonlinear when the input and output envelopes are considered. A general quantitative condition, valid for any kind of system, has been found that assures the linear processing of the envelopes and it has been shown that actually one of the inputs

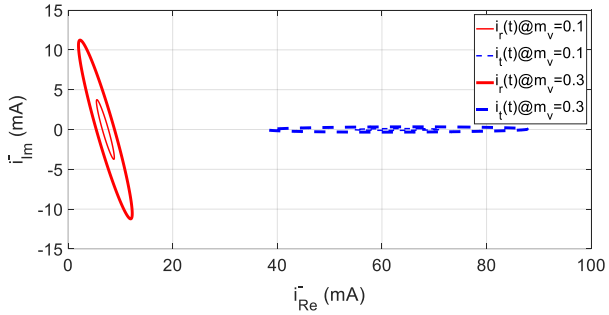

Fig. 13. Trajectories of the tips of $\bar{\imath}_t(t)$ and $\bar{\imath}_r(t)$ in R2 for $m_x = 0.1$ and $m_x = 0.3$.

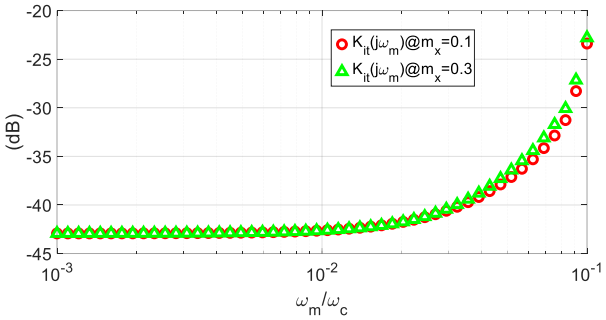

Fig. 14. Magnitude eBode diagrams obtained from the EM (lines) and by simulation.

of the converter fulfills the condition while the other does not. The effects of the latter situation on the envelope of the output signal have been analyzed in details obtaining general mathematical expressions that relate them to the characteristics of the TFs of the original system.

References

[1] S.R. Sanders, J.M. Noworolski, X.Z. Liu, and G.C. Verghese,"Generalized averaging method for power conversion circuits," *IEEE Trans. Power Electron.*, vol. 6, no. 2, pp. 251-259, April 1991.

[2] J. Mahdavi, A. Emaadi, M. D. Bellar and M. Ehsani, "Analysis of power electronic converters using the generalized state-space averaging approach," *IEEE Trans. Circuits Syst. I. Fundam. Theory Appl.*, vol. 44, no. 8, pp. 767-770, Aug. 1997, doi: 10.1109/81.611275.

[3] C.T. Rim and G.H. Cho, "Phasor transformation and its application to the DC/AC analyses of frequency phase-controlled series resonant converters (SRC)," *IEEE Trans. Power Electron.*, vol. 5, pp. 201–211, April 1990.

[4] C. T. Rim, "Unified General Phasor Transformation for AC Converters," *IEEE Trans. Power Electron.*, vol. 26, no. 9, pp. 2465-2475, Sept. 2011.

[5] C. Park, S. Lee, G. Cho and C. Rim, "Static and dynamic analyses of three-phase rectifier with LC input filter by laplace phasor transformation," in Proc. 2012 IEEE Energy Conversion Congress and Exposition (ECCE), 2012, pp. 1570-1577.

[6] M. Forato, M. Bertoluzzo and G. Buja, "Modeling of the dynamics of a resonant wireless power transfer circuit," in Proc. IEEE Int. Symposium on Industrial Electronics (ISIE), 2017, pp. 472-477.

[7] M. Forato, M. Bertoluzzo and G. Buja, "Dynamic EV Charging WPT System Control Based on Modulated Variable Laplace Transform," in Proc. IEEE PELS Workshop on Emerging Technologies: Wireless Power Transfer, 2018, pp. 1-6.

[8] M. Forato, "Dynamic wireless charging of electric vehicles", Ph.D. Thesis. University of Padova. Available: http://paduaresearch.cab.unipd.it/11411/1/forato_mattia_tesi.pdf.

[9] R. K. Jha, G. Buja, M. Bertoluzzo, S. Giacomuzzi and K. N. Mude, "Performance Comparison of the One-Element Resonant EV Wireless Battery Chargers," *IEEE Trans. Ind. Appl.*, vol. 54, no. 3, pp. 2471-2482, May-June 2018.

[10] G. Buja, M. Bertoluzzo and K. N. Mude, "Design and Experimentation of WPT Charger for Electric City Car," *IEEE Trans. Ind. Electron.*, vol. 62, no. 12, pp. 7436-7447, Dec. 2015.

[11] W. Zhang, S. Wong, C. K. Tse and Q. Chen, "Design for Efficiency Optimization and Voltage Controllability of Series–Series Compensated Inductive Power Transfer Systems," *IEEE Trans. Power Electron.*, vol. 29, no. 1, pp. 191-200, Jan. 2014.

[12] S. Lee, B. Choi and C. T. Rim, "Dynamics Characterization of the Inductive Power Transfer System for Online Electric Vehicles by Laplace Phasor Transform," *IEEE Trans. Power Electron.*, vol. 28, no. 12, pp. 5902-5909, Dec. 2013.